Hot-carrier luminescence in Si

Jeff Bude

Beckman Institute for Advanced Science and Technology, University of Illinois at Urbana-Champaign, Urbana, Illinois 61801

Nobuyuki Sano and Akira Yoshii

NTT LSI Laboratories, Nippon Telegraph and Telephone Corporation, Atsugi-shi, Kanagawa, 243-01 Japan

There has been a renewed interest in the spectra of emitted light from Si metal-oxide-semiconductor field-effect transistors (MOSFET's) in the belief that a better understanding of this phenomenon will lead to a deeper understanding of hot carriers in these devices. In this paper, we attempt to explain the physical mechanisms responsible for the light emission in Si under varying doping and carrier conditions and as a function of hot-carrier distribution functions. Based on this study, we have found that a proper inclusion of a realistic band structure is essential for the study of hot-carrier luminescence in Si. Furthermore, by including these band-structure effects, we conclude that the dominant light-emission mechanism in normally biased Si MOSFET's is a combination of direct and phonon-assisted inter-conduction-band radiation.

I. INTRODUCTION

Recently there have been many attempts to understand the spectra of emitted light from Si metal-oxide-semiconductor field-effect transistors (MOSFET's) because a proper interpretation of these spectra may offer a deeper understanding of the physics of hot carriers in these devices. Unfortunately, there is no consensus as to the dominant mechanism responsible for the emitted light. Three theories have been proposed to explain this phenomenon: phonon-assisted indirect recombination, direct hole to hole band transitions, and hot-carrier bremsstrahlung.[1−3] Only qualitative calculations have been performed that have assumed very simple band structures (parabolic-spherical bands) and have neglected transition matrix elements altogether. The relative importance of the emission mechanisms cannot be ascertained from these models. Furthermore, because the carriers in the emission processes are typically hot carriers, realistic band structures should be considered. Therefore these simple models are not adequate to explain the experimental results.

This paper attempts to construct a theoretical model which includes a realistic band structure and quantifies the relative importance of the different luminescence mechanisms in Si. Because of the structural complexity and extreme range of electric fields present in Si MOSFET's, it is necessary to consider a wide range of doping densities, carrier densities, and carrier distribution functions, and so the calculations presented here attempt to cover this range of possibilities.

The following is an outline of the topics covered here. Section II provides a survey of the possible emission mechanisms. Section III gives an analytic treatment for these mechanisms, and Sec. IV presents the computational model based on this treatment. In Sec. V, the results of the calculations are presented and discussed, and Sec. VI gives the conclusions based on these calculations.

II. CLASSIFICATION OF LUMINESCENCE MECHANISMS

In general, there are two important types of photo-emission mechanisms in semiconductors: radiative recombination involving both carrier types, and radiative transitions which involve only one type of carrier. The former will be referred to as conduction-band to valence-band (c-v) radiation, and the latter as either conduction to conduction-band (c-c) or valence to valence-band (v-v) radiation.

These processes can be further broken down into either direct transitions in which a single photon provides both energy and momentum conservation, or indirect transitions in which a photon provides the energy and an auxiliary interaction provides the momentum. The distinctions between direct and indirect c-c and c-v luminescence are shown in Fig. 1. The two most important types of indirect light-emission mechanisms present in Si are phonon-assisted (PA) and ionized impurity-assisted (IA) mechanisms since they are the dominant scattering mechanisms in Si devices.

In contrast, previous works offer a slightly less general description of the possible light-emission mechanisms. For instance, only PA c-v transitions are considered to contribute to indirect recombination, and IA mechanisms are assumed to dominate the indirect c-c and v-v transitions, and PA c-c and v-v mechanisms are ignored. Furthermore, the IA c-c (or v-v) emissions are referred to as bremsstrahlung radiation in analogy with the classical theory of bremsstrahlung radiation which results from the acceleration of electrons due to the Coulomb field of the ions. However, the classical theory of bremsstrahlung radiation has little applicability in a crystalline environment in which the band structure differs significantly from that of a free particle. Direct c-c emissions are usually not even considered. In this paper, the general approach above is adopted in order to treat all of the impor-
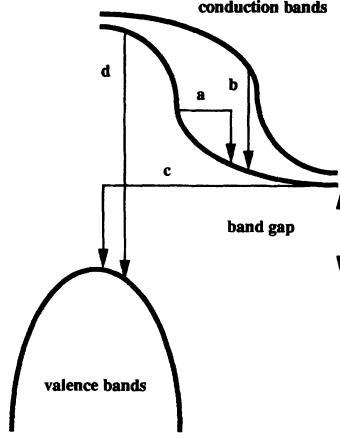
FIG. 1. Distinction of various luminescence mechanisms in a realistic band structure. (a) Indirect c-c, (b) direct c-c, (c) indirect c-v, (d) direct c-v.

tant sources of light emission in Si.

The qualitative spectra of the c-v radiation differ significantly from either c-c or v-v radiation, especially near the band-gap energy. In a c-v transition, there can be no significant radiation more than one-tenth of an electron volt below the band gap, and in general, the spectrum peaks at an energy slightly greater than the band-gap energy. In a c-c or v-v spectrum, no such dramatic peak is present near the band-gap energy. Hence, if a c-v transition is dominant, the spectra will clearly show a threshold behavior. However, without detailed calculations, nothing further can be said with reasonable accuracy concerning the emission spectra.

III. LUMINESCENCE THEORY

The Hamiltonian for an electron in a crystal coupled to the radiation field through the vector potential $\mathbf{A}(\mathbf{r},t)$ can be written as

$$H = \frac{1}{2m}\left[\mathbf{p} - \frac{e}{c}\mathbf{A}(\mathbf{r},t)\right]^2 + V_c(\mathbf{R}) ,$$ (1)

where V_c is the crystal potential. For our considerations the radiation field is small and can be treated as a perturbation on the Bloch wave function Ψ_{nk}. We keep only the term linear in the field, and write the photon perturbation H_{op} as[5]

$$H_{op} = -\frac{e}{mc}\mathbf{p}\cdot\mathbf{A}_\lambda = -i\frac{\hbar e}{mc}\nabla\cdot\mathbf{A}_\lambda .$$ (2)

The λ subscript refers to the polarization of the radiation field. Auxiliary perturbations must be included in the case of indirect photon emission.

In order to calculate the differential emission intensity $I(\hbar\omega)d(\hbar\omega)$ for the different light-emission mechanisms, we calculate the spontaneous-emission rate for these mechanisms since it is directly proportional to $I(\hbar\omega)d(\hbar\omega)$ for the case of negligible free-carrier absorption and low optical intensity.[6] Without these assumptions, direct comparison to experiment is very difficult. If, however, the emission takes place close to the surface of the sample and the carrier densities are not extremely high, then these assumptions are probably good and only a small fraction of the emitted light is reabsorbed. Furthermore, in order to compare the theory with experiment we must also assume that the experimental data have been properly normalized for transmission through the poly-Si. Throughout this paper we shall assume that the above conditions hold and evaluate the spontaneous-emission rate R.

If we denote the distribution function for electrons of band index i and wave vector k as $f(E_i(k))$, then the emission rate R, summed over all electron states and photon polarizations λ, can be written

$$R = \omega\frac{\Gamma}{4\pi}\sum_{u,l}\int d\Omega_\omega \sum_{\lambda,k_u,k_l} M_\lambda(u,l,k_u,k_l,\omega)f_u(E_u(k_u))$$

$$\times f_l(E_l(k_l))\delta(E_f - E_i) ,$$ (3)

where the indices u and l designate the upper and lower band indices for the transition $\bar{f}\equiv 1-f$, and Γ is a constant proportional to the product of the optical density of states. The integral over Ω_ω spans the angular coordinates of the radiation field, and M represents the appropriate matrix element for either the direct or indirect case.[6] The argument of the δ function is the difference in the initial and final energies of the system comprising the crystal and the radiation field.

Utilizing the 48-fold symmetry of the diamond lattice, we can perform the optical angular integral and the sum over polarizations by reducing one of the wave-vector sums over the Brillouin zone (BZ) into one over an irreducible wedge (RZ). Then, converting the wave-vector sums into integrals by introducing the crystal volume V, the spontaneous-emission rate for direct transitions R_{dir} becomes

$$R_{dir}(\omega) = 32\omega\Gamma\sum_{ul}\frac{V}{8\pi^3}\int_{RZ}d^3k\, f_u(E_u(k))\bar{f}_l(E_l(k))\sum_{i=1}^{3}|\langle u|\nabla_i|l\rangle|^2\delta(E_l(k) - E_u(k) + \hbar\omega) .$$ (4)

Note that for the direct transitions, $k_u = k_l$ (neglecting the momentum of the photon) in order to satisfy the momentum-conserving optical matrix element. Thus direct transitions are vertical transitions between electrons of different bands. For the case of Si, direct c-v-type transitions will occur for photon energies greater than the direct-band-gap energy, which is about 3.2 eV. Most experiments measure radiation substantially less energetic than this, so if experimental spectra contain radiation from direct transitions for energies less than 3.2 eV, then this radiation will be either c-c or v-v radiation.

A similar expression is derived for indirect radiation, but both integrals over the upper and lower wave vectors

remain because H_p removes the $k_u = k_l$ restriction. The indirect-photon-emission rate R_{in} is given by

$$R_{in}(\omega) = 32\omega\Gamma \sum_{ul} \frac{V^2}{(8\pi^3)^2} \left[\int_{RZ} d^3k_l S_l(\omega, k_l) \int_{BZ} d^3k_u + \int_{RZ} d^3k_u S_u(\omega, k_u) \int_{BZ} d^3k_u \right]$$

$$\times \bar{f}_l(E_l(k_l)) f_u(E_u(k_u)) |\langle k_u | H_p | k_l \rangle|^2 \delta_{if} \ , \tag{5}$$

with the definitions

$$S_n(\omega, k) = \sum_{i=1}^{3} \left| \sum_m \frac{\langle mk | \nabla_i | nk \rangle}{E_n(k) - E_m(k) - \hbar\omega} \right|^2 , \tag{6}$$

$$\delta_{if} = \delta(E_l(k_l) - E_u(k_u) + \hbar(\omega + \omega_q))$$
$$+ \delta(E_l(k_l) - E_u(k_u) + \hbar(\omega - \omega_q)) \tag{7}$$

for PA emission and

$$\delta_{if} = \delta(E_l(k_l) - E_u(k_u) + \hbar\omega) \tag{8}$$

for IA emission. $\hbar\omega_q$ is the photon energy for an assisting-phonon wave vector $q = k_u - k_l$. The term with a summation over matrix elements between intermediate states, (6), arises from second-order perturbation theory in which a virtual transition relaxes the momentum-conserving requirement between the initial and final states.

Care must be taken with these matrix-element sums since, if the denominators vanish, the sums will not converge and second-order perturbation theory breaks down. This occurs when one of the virtual states becomes a real state, which is possible in the present context for either c-c or v-v transitions.

However, even in these cases, the perturbation theory is not divergent if we look at the exact form second-order perturbation takes before the "golden-rule" approximation is applied. In this case, the sum over intermediate states can be converted into an integral, and the true expression for the matrix element involves a principal-value integral over intermediate states which excludes the pole in the denominator.[7] Furthermore, the Bloch states are not exact eigenstates due to phonon scattering and have a finite lifetime corresponding to a nonzero width in energy space. When the principal-value integral over intermediate states having nonzero width is evaluated, it is found that terms in the matrix element for which the denominator is very small are actually suppressed and vanish when there is a pole.[8] Therefore, when performing the summation in $S_n(\omega, k)$, those terms for which the denominator approaches the energy width of the state involved should be taken out of the sum since they do not contribute when the full expression for the matrix element is considered.

In order to evaluate the above expressions, a proper form must be found for the distribution functions. When the carriers are in a high electric field, one usually assumes that the distribution departs from the equilibrium distribution (Maxwell-Boltzmann) through an increase in the carrier temperature.[9] Throughout this paper, this form for the distribution function will be referred to as the temperature model. If degeneracy effects are negligible, the temperature model distribution function can be

expressed as

$$f(E) = N(T_c, n) e^{-E/k_B T_c} , \tag{9}$$

where T_c is the carrier temperature, k_B is Boltzmann's constant, and n normalizes the distribution for the given carrier density n. The relationship between N and f takes the form

$$N(T_c, n) \int dE \sum_i g_i(E) f(E) = n , \tag{10}$$

where g_i are the densities of states for the bands i in the appropriate energy range. If degeneracy effects can be neglected and $N \ll 1$, $\bar{f} = 1 - f \approx 1$.

However, there is evidence from Monte Carlo calculations that a considerable departure from the temperature model occurs under extremely high field conditions.[10,11] When $F > 10^5 V$/cm, the distribution becomes nearly flat for low energies and exponential for high energies, and can be represented empirically by a function of the form

$$f(E) = N(A, B, n) \exp(-AE - BE^2) , \tag{11}$$

where the normalization $N(A, B, n)$ is calculated as in (10) above. The effect of this distortion is important when measuring luminescence under high field conditions.

IV. COMPUTATIONAL MODEL

To implement the above expressions in a computational model, a pseudopotential band structure (see, for example, Ref. 12) including energy derivatives and eigenfunctions for the eight lowest bands was calculated for 2972 points in the irreducible wedge defined by

$$0 \le k_z \le k_y \le k_x \le \frac{2\pi}{a}, \quad k_x + k_y + k_z \le \frac{3\pi}{a} , \tag{12}$$

with mesh spacing equal to one-thirtieth of $2\pi/a$. From this band structure, the density of states (DOS) was calculated using the expression

$$g_i(E) = \int_{BZ} d^3k \ \delta(E - E_i(k)) . \tag{13}$$

The normalization factors N for the distribution functions (10) were calculated using these DOS.

Then, the matrix elements for the direct- and indirect-spontaneous-emission rates were calculated using the pseudopotential wave function. For example,

$$\langle mk' | \nabla_i | nk \rangle = \delta_{k,k'} \int_{BZ} d^3r \ u_{mk'}^*(r) \nabla_i u_{nk}(r)$$
$$+ \delta_{k,k'} ik \int_{BZ} d^3r \ u_{mk'}^*(r) u_{nk}(r) . \tag{14}$$

Because $\omega \ne 0$ and $m \ne n$, the second term in (14) is zero.

The Bloch functions can be expanded in a series of reciprocal-lattice vectors G_j,

$$\langle r|nk \rangle = e^{ik\cdot r}\sum_j z_j(nk)e^{iG_j\cdot r} , \qquad (15)$$

because they are periodic in lattice translations. Substituting (15) into (14),

$$\langle mk'|\nabla_i|nk \rangle = \delta_{k'k}\sum_j z_j^*(mk')z_j(nk)G_j . \qquad (16)$$

These matrix elements were calculated for every mesh point for the direct-emission case and were found to vary over an order of magnitude or more along different directions in the RZ. However, the matrix-element sums for the indirect cases were calculated only as functions of photon energy and band indices, as they varied little as a function of position in the RZ.

Then, integrals over the RZ were evaluated as follows:

$$\int_{RZ}d^3k \rightarrow \sum_{k^0\in RZ}\int_{k^0-\Delta}^{k^0+\Delta}d^3k\, W(k) , \qquad (17)$$

where k^0 are mesh points, and Δ is one-half of the mesh spacing. $W(k)$ is the fraction of each mesh cell within the RZ. Matrix elements were assumed constant within each mesh cell. Exact analytic expressions for the above mesh-cell integrals were obtained from the properties of the δ functions and the analytic forms for the distribution functions.

Then, for the indirect cases, analytic forms were assumed for the auxiliary perturbation matrix elements,

$$K(k_u,k_l)\equiv|\langle k_u|H_p|k_l \rangle|^2 , \qquad (18)$$

and defining M_{av} as the average matrix element sum, the spontaneous-emission rate for the indirect cases was approximated,

$$R_{in} \propto \sum_{ul}\sum_{k^0\in RZ}\int_{k^0-\Delta}^{k^0+\Delta}d^3k_l\,W(k_l)\bar{f}_l M_{av}(k_l,k_u,\omega)$$

$$\times[J_u(k^0)+k_l\cdot\nabla J_u(k^0)] , \qquad (19)$$

with

$$J_i(k^0)\equiv \sum_{k_i^0\in BZ}\int_{k^0-\Delta}^{k^0+\Delta}d^3k_i\,W(k_i)f_i(E_i(k_i))\delta_{if} . \qquad (20)$$

In the expression for R_{in}, J is expanded to first order in K_l in each mesh cell.

The following models were assumed for $K(k_u,k_l)$: for phonons, the standard form used in Monte Carlo simulations was used for the matrix elements, with a proper weighting between f- and g-type intervalley scattering. The typical Monte Carlo model assumes

$$K(k_u,k_l)=\frac{\hbar}{2\rho\omega_q}N(\omega_q)D^2 , \qquad (21)$$

with different coupling constants D for each contributing phonon.[9] In this model, ρ is the density of the material, and N is the equilibrium phonon number from the Bose-Einstein distribution. The values for D were taken from Ref. 13. This is rather phenomenological, however it

should give a right order of magnitude for the PA rate. Any improvement in the form for $K(k_u,k_l)$ requires extensive computation using the rigid pseudoion approximation for the electron-phonon matrix elements (see Ref. 14). It is unclear whether the improvement would warrant the substantial effort involved in this type of calculation.

The screening of the ions due to both the valence electrons and the mobile charges is included here through the use of the random-phase approximation wave-vector-dependent dielectric function $\epsilon(q,0)$ (see Ref. 16); the screening due to the mobile charges is provided by a Thomas-Fermi screening wave vector.[5] The resulting impurity matrix element is of the Brooks-Herring form.[15] The use of the Thomas-Fermi screening wave vector is strictly valid only in near equilibrium situations. However, as will be demonstrated, impurity associated radiation is only significant in very highly doped regions of a device, which are typically the contacts. In these regions, a high-temperature electron distribution is injected into the contact and rapidly cools. The impurities there are screened by the contact electrons which are in quasiequilibrium, so the Thomas-Fermi screening wave vector is applicable in this important case. In more general situations, a much more detailed analysis is needed.

The frequency dependence of the dielectric function is not included, since up to $\omega=3$ eV, there is little variation in $\epsilon(q,\omega)$.[16] However, there is a large variation with wave vector. Typically, the small-q limit for the static dielectric function $\epsilon(q,0)$ is used in the Brooks-Herring model, i.e., $\epsilon(0,0)=\epsilon_r$. On the scale of $2\pi/a$, $\epsilon(q,\omega)$ varies considerably (from 11.7 to 1), and can offset the increased probability for scattering for small q. This is important in calculating IA transitions which necessarily require large q—the inclusion of the real dielectric function increases the IA scattering by factors as high as 3 compared to the traditional approach. The matrix-element form for ionized impurity matrix elements used in our simulation is given by

$$K(k_u,k_l)=\frac{e^2}{\epsilon_r^2}\frac{N_I}{\left[\dfrac{\epsilon(q,0)}{\epsilon_r}|k_u-k_l|^2+q_0^2\right]^2} , \qquad (22)$$

where q_0 is the Thomas-Fermi screening length, and N_I is the dopant density.

V. RESULTS AND INTERPRETATIONS

Our results are shown in Figs. 2–4, 6(a), 6(b), and 8. The "relative intensity" used for intensity is common, so that comparisons between graphs is possible. The plots for "normalized intensity" have been normalized to compare to experiment. Furthermore, for all figures, the differential intensity curves scale by the following rules, where I_0 is the plotted intensity and I is the actual intensity. Here, n and p are the free-carrier densities for electrons and holes, respectively, and N_I is the impurity density. For c-c emission,

$$I = \frac{n}{10^{15} \text{ cm}^{-3}} I_0 , \qquad (23)$$

and for c-v emission,

$$I = \frac{n}{10^{15} \text{ cm}^{-3}} \frac{p}{10^{15} \text{ cm}^{-3}} I_0 . \qquad (24)$$

For IA emission, which scales with N_I, the additional rule applies:

$$I = \frac{N_I}{10^{20} \text{ cm}^{-3}} I_0 . \qquad (25)$$

Furthermore, if these results are to be applied to spatially varying situations, we must use

$$I_{\text{tot}} = \sum_i \int d^3 r \, I_i(T(r)) n(r) p(r) , \qquad (26)$$

where I_i is the emission intensity profile for the ith luminescence mechanism.

First, general results for the temperature model are presented. Then, more general distributions and experimental comparisons are presented.

A. Electron temperature model — general trends

Figure 2 shows the temperature model luminescence spectra for direct and PA c-c radiation for $T_c = 500$–1700 K in increments of 300 K and a lattice temperature of $T_L = 300$ K demonstrating several important features about these two types of spectra. First, the emission intensity of c-c radiation increases rapidly as a function of temperature. Also, at $T_L = 300$ K, direct c-c radiation is dominant for the lower end of the spectrum, whereas PA emission dominates for higher photon energies. This reflects the general trend that direct c-c emission decreases more rapidly than indirect c-c due to the additional constraint of crystal momentum conservation.
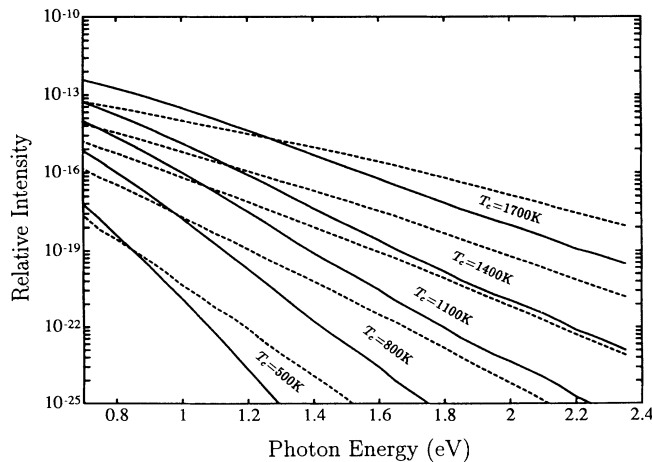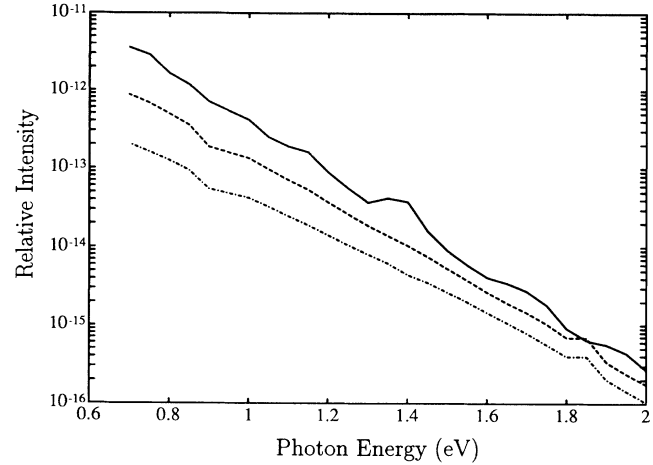
Figure 3 shows the photoluminescence associated with

FIG. 3. Calculated spectra for IA c-c (bremsstrahlung) radiation as a function of the mobile screening charge density n for $T_c = 1700$ K and $N_I = 10^{20}$ cm^{-3}; solid curve, $n = 10^{18}$ cm^{-3}; dashed curve, $n = 10^{19}$ cm^{-3}; dash-dotted curve, $n = 10^{20}$ cm^{-3}.

IA indirect c-c processes for $T_c = 1700$ K. The three curves plotted correspond to any impurity density of $N_I = 10^{20}$ cm^{-3} with screening densities of $n = 10^{18}$, 10^{19}, and 10^{20} cm^{-3} from top to bottom. Lower mobile charge screening densities lead to greater increases in the slope of the spectrum because of the divergent character of the ionized impurity matrix element (22). It is important to notice, however, that these spectra scale with N_I as in (25). Therefore, comparing Fig. 3 with Fig. 2, it is apparent that for elevated T_c and when $n = N_I$, ionized IA c-c emission intensity cannot compete with PA or direct c-c unless $N_I \geq 5 \times 10^{20}$ cm^{-3} where the validity of (22) is certainly questionable.

IA luminescence is small compared to PA c-c because, for large $\hbar\omega$, the crystal momentum supplied by either the impurity or the phonon must be large—this is a characteristic of the Si band structure. This forces $q = |k_u - k_l|$ to be large in (22); hence the impurity matrix element is small. Even including the effects of valence-band screening [$\epsilon(q,0)$], the impurity matrix element will be much smaller than the phonon matrix element, which is fairly insensitive to q for hot electrons. Even if T_L is very small, forcing the phonon matrix elements to go to zero, direct emission persists and still dominates the IA emissions. This contradicts the commonly held belief that IA c-c (bremsstrahlung radiation) is a dominant mechanism in hot-electron emission spectra. The above considerations carry over to the v-v case with almost no significant modifications.

Figure 4 shows the temperature model spectra for PA c-v radiation at $T_L = 300$ K. c-v spectra differ significantly from c-c or v-v in several respects. First, the emission spectra for c-v emission drops rapidly to zero for $\hbar\omega$ more than a phonon energy below the band-gap energy E_G. Also, the maximum intensity for a given T_c occurs roughly at 1.1 eV. Furthermore, for high T_c, there is virtually no increase in the maximum intensity as a function of T_c, whereas for c-c emission near 1.1 eV,

FIG. 2. Calculated spectra for direct (solid curve) and PA (dashed curve) c-c radiation as a function of the electron temperature T_c at $T_L = 300$ K.
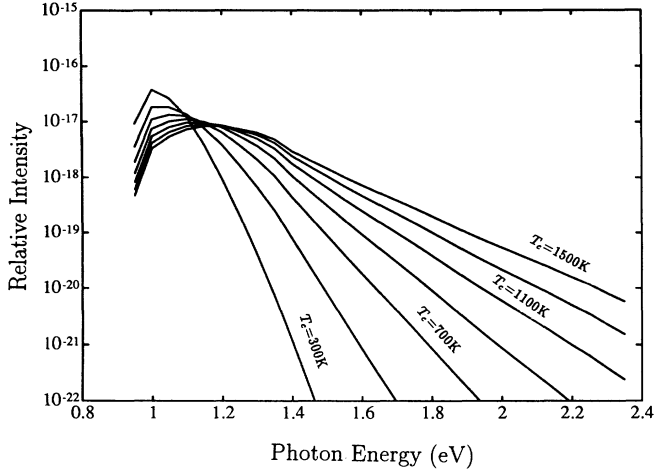
FIG. 4. Calculated spectra for PA c-v radiation as a function of the T_c for $T_h = T_L = 300$ K.

there is an exponential decrease in intensity as a function of T_c. In fact, for c-v emission, the maximum intensity is even insensitive to the hole temperature T_h. Most important, however, is the fact that for hot electrons, c-v emission intensity is many order of magnitude less than c-c. For hot-electron c-v radiation to compete with c-c radiation [see the scaling rules (23) and (24)], the hole density must be at least 10^{19} cm^{-3} or more, which is usually an impractical requirement. IA c-v emission suffers from the same problem as IA c-c emission, because the indirect X-Γ transition also requires large q for $\hbar\omega < 3$ eV, and so it can usually be neglected.

B. Gaussian distributions

As mentioned before, Monte Carlo simulations have pointed out that the distribution function may differ significantly from the hot-electron temperature model in
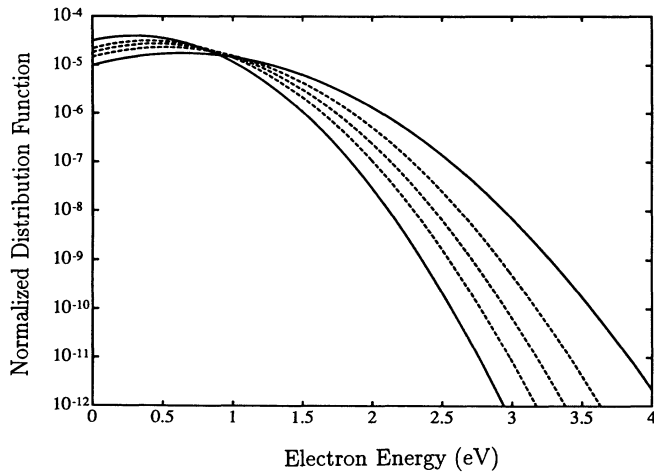

FIG. 5. Normalized Gaussian distributions. Upper solid curve: fit to Higman et al. data, $A = -1.82$, $B = 1.41$. Lower solid curve: fit to Sano et al. data, $A = -1.49$, $B = 2.50$. Dashed curves: intermediate Gaussians with $A = -1.82$ and $B = 2.25, 2.00$, and 1.75.

very high field situations such as those associated with impact ionization. Higman et al.[10] and Sano et al.[13] have presented high field distributions calculated using Monte Carlo simulators near the drain region of Si MOSFET's; see Fig. 5. (Note that these have been normalized against the density of states.) These spectra have been fitted to the Gaussian form (11), and luminescence spectra for the c-c and v-v processes have been calculated. The results for c-c emission are shown in Fig. 6 along with several spectra for distributions whose shapes are intermediate compared to the simulated spectra of Refs. 10 and 13. The emission spectra for c-v luminescence are quite similar to the temperature model in the extremely high T_c case. In fact, for the distributions of Fig. 6, c-v
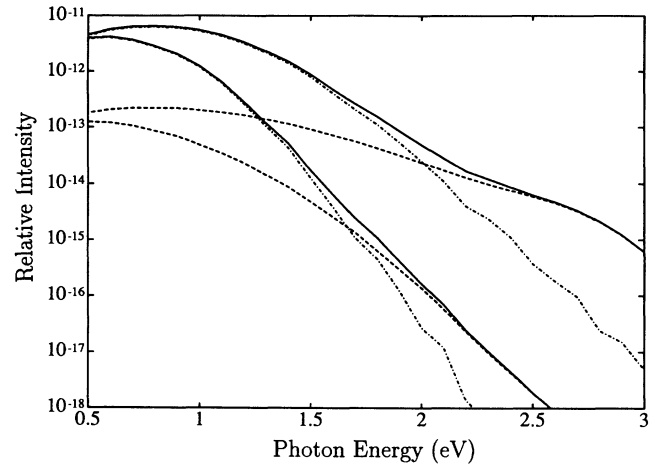
(a)
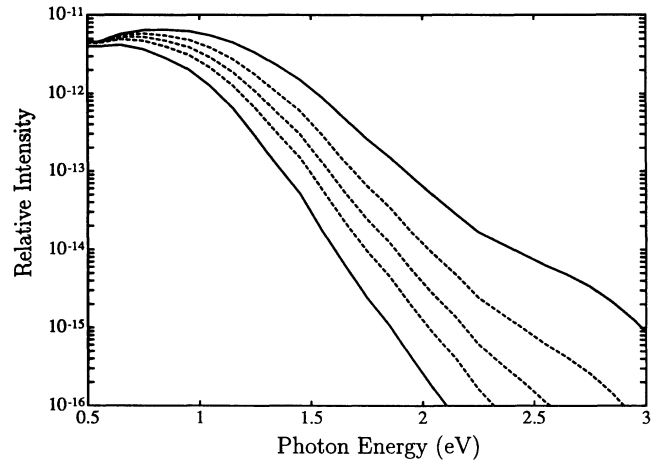
(b)

FIG. 6. (a) Calculated c-c spectra for solid curves in Fig. 5 with $T_L = 300$ K. The upper set of curves corresponds to the data of Higman et al., and the lower set of curves to Sano et al. Dash-dotted curves, direct c-c; dashed curves, PA c-c; solid curves, sum of direct and PA c-c. (b) Calculated c-c spectra (sum of direct and PA) for distributions in Fig. 5 with the same ordering as in Fig. 5 [i.e., top curve in (b) corresponds to the top curve in Fig. 5, etc.].

luminescence is nearly flat out to $\hbar\omega = 3.0$ eV, decaying by factors of 10 or 100 compared to the many orders of magnitude characteristic of the c-c emission in Fig. 6. Just as in the temperature model case, c-v emission in the Gaussian limit has a maximum intensity near the band-gap energy which is five to six orders of magnitude less than the peak values in for the corresponding c-c emission spectra.

C. Comparison to experiment

Experimental results are shown in Fig. 7. The dashed and the dash-dotted curves are early results for Si p-n-junction diodes from Chynoweth and McKay.[17] They are representative of p-n-junction photoluminescence data (see Refs. 18 and 19). The dashed curve corresponds to forward bias and the dash-dotted curve corresponds to a high reverse bias inducing avalanche breakdown in the junction. These results are consistent with the observations above. In particular, in forward bias, there is a high density of injected holes and electrons in the junction region, but the carrier distributions are not heated since the electric field is small. Therefore $T_c \approx T_h \approx T_L = 300$ K. From Fig. 2, the maximum c-c intensity should be much less than 10^{-20}, whereas from Fig. 4, the c-v curve has a maximum near 10^{-17}. In fact, these figures indicate that c-v emission will dominate c-c emissions over the entire frequency range observed. This is in fact the case for the experimental results shown in Fig. 7. The dotted curve corresponds to the $T_c = 300$ K c-v distribution in Fig. 4. In the reverse biased case, both the hole and electron distributions should be heated. In fact, for fields high enough to produce significant ionization ($F > 10^5$ V/cm), the Monte Carlo distributions of Fig. 5 should apply. The resulting luminescence curves in Fig. 6 compare favorably with reversed biased result. However, Fig. 6

FIG. 7. Experimental results: Solid curve, Si MOSFET from Toriumi et al.; dotted curve, Si MOSFET from Das and Arora; dashed curve, forward biased Si p-n-junction diode from Chynoweth and McKay; dash-dotted curve, reverse-biased Si p-n-junction diode in the breakdown region from Chynoweth and McKay.

indicates that the mechanism responsible for the emission is a combination of direct and PA c-c (and v-v) radiation, whereas most earlier studies based on less rigorous models predict the reverse-biased emissions to be the result of bremsstrahlung and recombination (c-v).

Early studies of the total (integrated) light emission for n-channel Si MOSFET's have shown a strong correlation between the substrate electron current and the intensity as a function of bias conditions.[20,4] The explanation given by Childs, Eccleston, and Stuart was that the electron substrate current was generated by photons absorbed in the substrate, implying that the light emission was a hot-electron effect (a significant portion of the emitted light exceeded the band-gap energy and therefore was generated by hot electrons). The first analysis of the spectral content of the radiation from a 1.5-μm Si MOSFET operated in the current saturation region is plotted as the solid curve in Fig 7. These data show an almost exponential decay with a characteristic temperature of 1600 K in the region $1.7 \leq \hbar\omega \leq 2.5$ eV, demonstrating the important role of hot-electron transitions in the light emission. Tsuchiya and Nakajima argued that the emitted light from a similar structure was a result of the recombination of avalanche generated electron-hole pairs near the drain. That this is unlikely follows from the hot-carrier light-emission analysis above: since the hole densities are certainly less than 10^{19} cm^{-3}, c-v emission cannot compete with c-c or v-v emission. v-v emission can be ruled out because the nonequilibrium holes are present only in small densities near the drain where they are produced by impact ionizing electrons from the channel, whereas the density of hot electrons from the channel is large. Therefore the radiation is most likely c-c emission from the high field region near the drain. [The c-c spectrum will be dominated by the emission from regions with high field distributions (near the drain) because c-c emission intensity is a strong function of T_c.] Toriumi et al. have explained the spectrum of Fig. 7 as resulting from ionized impurity c-c emission (bremsstrahlung) because of shape of the emission profile. Note, however, that the simple exponential dependence of the bremsstrahlung spectrum that they use is a result of several crude approximations concerning the shape of the distribution function, the band structure, and the ionized impurity interaction itself Also, the nearly Maxwell-Boltzmann shape of the spectrum in this region is not necessarily an indication that the hot-electron distribution is Maxwell-Boltzmann. Several of the calculated emission profiles in Fig. 6 corresponding to various Gaussian-shaped distributions show this same behavior in the region $1.7 \leq \hbar\omega \leq 2.5$ eV because of the coexistence of both direct and PA c-c. In fact, the curve in Fig. 6 corresponding to $A = -1.82$ and $B = 2.0$ in (11) fits the experimental spectrum rather well. Therefore we propose that the Si MOSFET spectrum of Toriumi et al. is due to the coexistence of both direct and PA c-c. Furthermore, as discussed below, the calculated results here also explain the sub-band-gap emission where c-v cannot exist.

Figure 8 shows a comparison of the sub-band-gap emission in Si between this theory and experiment. The dash-dotted curve is an experimental result due to Her-
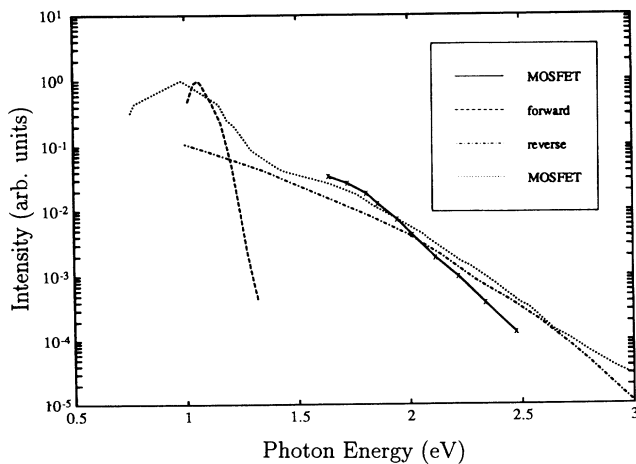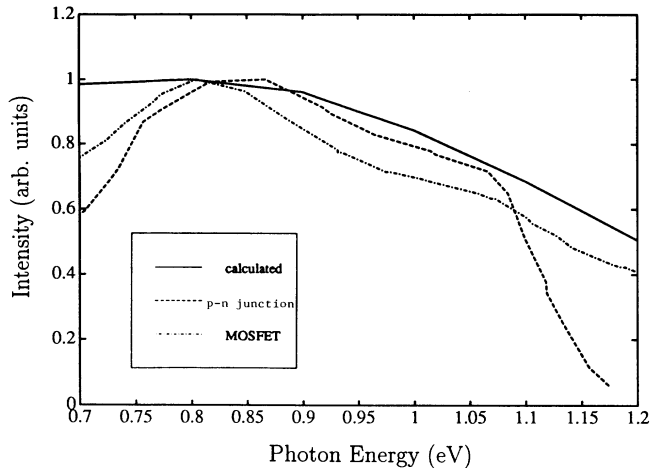
FIG. 8. Experimental and calculated spectra in the sub-band-gap region. Solid curve, calculated c-c spectrum from Fig. 6(b); dash-dotted curve, Si MOSFET from Herzog et al.; dashed curve, Si p-n-junction diode reverse biased in the break-

zog et al. for a Si MOSFET,[2] the dashed curve corresponds to reverse-biased Si p-n-junction emission due to Haecker,[18] and the solid curve is the calculated c-c spectrum of Fig. 6 corresponding to the Monte Carlo distribution of Higman et al.[10] The emission in all three is rather flat in the $0.6 < = \hbar\omega \leq 1.2$ eV range (notice the linear plot) with a slight peak near 0.8 eV. Note that Haecker explains this spectrum by direct v-v emission resulting from transitions to the split-off heavy-hole band; these transitions show a peak near 0.8 eV due to the energy dependence of the matrix element. However, as shown in Fig. 8, c-c emission with high field distributions can easily account for this peak. Furthermore, Haecker has not considered the fact that other hole to hole transitions must also be important when hot carriers are present, and they can mask any peaks due to the heavy-hole transitions.

Finally, we should comment on the peak structure of the MOSFET spectrum in the low-energy region in Fig. 7 produced by Das and Arora.[3] The spectrum for $\hbar\omega \geq 1.7$ eV corresponds roughly to the results of Toriumi et al. and the Gaussian spectra calculated in Fig. 6. This result even shows a slight flare-out for $\hbar\omega \geq 2.5$ eV anticipated by some of the broader distributions of Fig. 6. However, the spectrum in the low-energy region is difficult to interpret since it is dramatically different from the sub-band-

gap spectra plotted in Fig. 8. It may be a composite of emissions from two different regions in the MOSFET for the following reasons: first, if the hole and electron densities near the drain were high enough that c-v emission dominated (an unlikely event), then the distribution would be quite flat and would decay by a few orders of magnitude over the entire energy range measured. Since this is not the case, it is improbable that hot-carrier c-v emission is responsible for this result. As mentioned above, the higher end of the spectrum looks quite like the c-c hot-electron emissions of Fig. 6. The peak with the dropoff near the band-gap energy is characteristic of low-temperature c-v emission. Therefore we suggest that this peak is due to a high density of holes with $T_h \approx T_L$ recombining in the source where the electron density is quite high, $n_{source} \approx 5 \times 10^{20}$ cm^{-3}. The product of n and p in the source may then compensate for the marked difference in emission intensity between the c-c near the drain and the "cool-carrier" c-v recombination in the source. If the MOSFET was biased close to or in the breakdown region this is possible.

VI. CONCLUSIONS

We have presented the results of a rigorous model for hot-carrier luminescence in Si, and have recorded the relative importance of the various types of light emission over a wide range of conditions. Based on this model, we have found that processes such as inter-conduction-band luminescence resulting from the inclusion of a realistic band structure are dominant hot-carrier light-emission mechanisms in Si. Furthermore, we have found reasonable agreement with the experimental data from p-n-junction diodes and MOSFET'S, and have concluded that the radiation from n-channel MOSFET's is a result of the coexistence of direct and phonon-assisted conduction-band to conduction-band radiation We have also confirmed that the Gaussian-shaped distribution functions calculated by high field Monte Carlo simulations are responsible for the light emission in MOSFET's.

ACKNOWLEDGMENTS

[1]A Toriumi, M. Yoshimi, M. Iwase, Y. Akiyama, and K. Taniguchi, IEEE Trans. Electron. Devices 34, 1501 (1987).

[2]M. Herzog, M. Scehls, F. Koch, C. Moglestue, and J. Rosenzweig, Solid-State Electron. 32, 1065 (1989).

[3]N. C. Das and B. M. Arora, Appl. Phys. Lett. 56, 1152 (1990); 53, 2620 (1988).

[4]T. Tsuchiya and S. Nakajima, IEEE Trans. Electron. Devices 32, 405 (1985); Solid-State Electron. 32, 1065 (1989).

[5]B. K. Ridley, in Quantum Processes in Semiconductors (Clarendon, Oxford, 1988).

[6]H. Bebb and E. M. Williams, in Photoluminescence I: Theory, edited by R. K. Willardson and A. C. Beer, Semiconductors and Semimetals Vol. 8 (Academic, New York, 1972), p. 181.

[7]L. I. Schiff, Quantum Mechanics (McGraw-Hill, Tokyo, 1950), pp. 202–204.

[8]W. Heitler, The Quantum Theory of Radiation (Clarendon, Oxford, 1950), pp. 175–275.

[9]K. Hess, Advanced Theory of Semiconductor Devices (Prentice-Hall, Englewood Cliffs, NJ, 1987).

[10]J. Higman, K. Hess, C. Hwang, and R. Dutton, IEEE Trans.

Electron. Devices **36**, 930 (1989).

[11]M. V. Fischetti, S. E. Laux, and D. J. Dimaria, Appl. Surf. Sci. **39**, 578 (1989).

[12]M. L. Cohen and T. K. Bergstresser, Phys. Rev. **141**, 789 (1966).

[13]N. Sano, T. Aoki, M. Tomizawa, and A. Yoshii, Phys. Rev. B **41**, 12 122 (1990).

[14]See the chapters by J. Higman and J. Bude, in *Monte Carlo Simulations in Semiconductors* edited by K. Hess (Kluwer Academic, Boston, 1991).

[15]H. Brooks and C. Herring, Phys. Rev. **83**, 879 (1951).

[16]J. P. Walter and M. L. Cohen, Phys. Rev. B **5**, 3101 (1971).

[17]A. G. Chynoweth and K. G. McKay, Phys. Rev. **102**, 369 (1956).

[18]W. Haecker, Phys. Status Solidi A **25**, 301 (1974).

[19]J. Shewchun and L. Y. Wei, Solid State Electron. **8**, 485 (1965).

[20]P. A. Childs, W. Eccleston, and R. A. Stuart, Electron Lett. **17**, 281 (1983).